High-Efficiency Operation of an Open-Ended Winding Induction Motor Using Constant Power Factor Control

Ian J. Smith and John Salmon, *Member, IEEE*

***Abstract*—A controller is presented for an open-ended winding motor dual-inverter drive (DID), where main and floating inverters are supplied from a dc power source and a floating dc capacitor, respectively. The controller utilizes the efficiency characteristic of induction machines, where high power conversion efficiencies are obtained when operating the machine with a constant fundamental power factor, typically around 0.70–0.75, over a wide load range and under variable frequency. The controller uses the drive's topology to maintain the motor's desired power factor. In essence, the main inverter's output voltage is used to control the floating inverter's dc capacitor voltage to keep the injected fundamental voltages of both inverters at a desired ratio. The floating inverter's voltage is operated with a 90° lead relative to the main inverter and uses a constant maximum amplitude modulation depth to minimize the capacitor's operating voltage. This approach updates the motor's voltage automatically to ensure constant power factor operation and improves the floating capacitor's voltage stability during transient conditions. The inherent voltage-boosting capability of this topology is especially beneficial in extending the constant torque region of the motor and improving performance in the speed range extension region. Simulation and experimental results verify the predicted motor efficiency gains and stability under speed and load transients.**

***Index Terms*—Dual-inverter drive (DID), floating bridge, open-ended winding induction machine, power factor control, variable-frequency drive.**

I. Introduction

OVER the last decade, the open-ended winding induction machine (IM) and dual-inverter drive (DID) topology has gained attention as a practical high-efficiency variable-frequency motor drive system. The primary benefits of this drive include boosting of the motor's terminal voltage [1]–[8], a multilevel pulse width modulation (PWM) supply voltage with increased switching frequency [5]–[18], and improved motor performance in the speed extension region [2], [18]–[22]. The multilevel nature and the voltage-boosting capability of the DID make it ideal for medium-voltage and high-power applications or low-voltage applications demanding high frequencies [23]–[25].

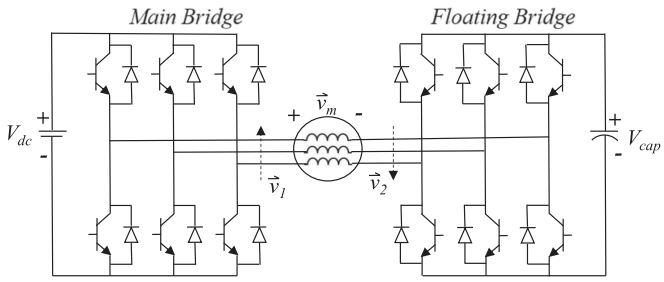

Fig. 1. DID with a floating capacitor bridge.

Various configurations of the DID exist, including topologies that use two isolated dc sources [15]–[17], [26], a single dc source supplying both inverters [1], [9]–[12], [27], [28], and a floating dc capacitor to supply the floating bridge [2]–[6], [21], [22] (see Fig. 1). Recently, the floating bridge topology has gained popularity in literature, as it eliminates the pathways for common-mode currents to circulate within the system [2]–[7], [18], [28], thus eliminating the need for bulky common-mode choke inductors or an additional level in the PWM control scheme to suppress these currents [1], [9]–[12], [18], [28]. In addition, the floating bridge topology reduces the size, weight, and cost of the system compared to a DID supplied by two isolated dc sources [1].

The DID topology with a floating bridge has been previously utilized to provide reactive motor voltage support and counteract supply voltage droop [4], provide five-level line voltages to the motor while regulating the capacitor voltage at 50% relative to the main dc supply voltage [5], [6], and provide flux-oriented control for high-speed applications [21], [22]. Furthermore, it has been shown that if left unregulated, the floating capacitor will naturally charge or discharge to a stable steady-state operating point depending on the motor's current loading conditions [2], [3].

The focus of the proposed control scheme is to maintain high motor power conversion efficiencies over a wide range of motor load settings and drive operating frequencies, while also providing voltage boosting for improved motor performance under high loads and in the speed range extension region. These benefits, along with the other inherent benefits of this topology, create an attractive motor drive system. Applications for

Manuscript received July 2, 2017; revised November 21, 2017; accepted February 2, 2018. Date of publication February 15, 2018; date of current version September 28, 2018. Recommended for publication by Associate Editor A. Mertens. *(Corresponding author: Ian J. Smith.)*

The authors are with the Department of Electrical and Computer Engineering, University of Alberta, Edmonton, AB T6G 2V6, Canada (e-mail: ijsmith@ualberta.ca; john.salmon@ualberta.ca).

Color versions of one or more of the figures in this paper are available online at http://ieeexplore.ieee.org.

Digital Object Identifier 10.1109/TPEL.2018.2806740

the proposed control include variable-frequency variable-torque industrial drive applications such as fans, pumps, and compressors. As many industrial drives have high capacity factors and long lifetimes, it is imperative to maintain high efficiencies independent of the operating point. In addition, the multilevel nature of this topology makes it suitable for medium- and high-power applications. The floating bridge DID topology has been demonstrated to have high power conversion efficiencies when operating the motor with a constant power factor control [29]. This paper presents a new controller with the following features: a noncomplex control structure, minimal feedback signals, utilization of the DID structure topology, and a variable floating bridge dc capacitor voltage that inherently changes with the motor's operating conditions (speed and load), hence improving the overall drive's power conversion efficiency. Theoretical and experimental motor efficiencies for the proposed control are compared to the theoretical maximum possible efficiencies for the machine based upon equivalent circuit model calculations. Experimental results for both load and speed transients demonstrate the control to be suitable for dynamic motor drive applications.

II. Principles of Operation

The operating principles of the DID system, which arise from the drive's topology, are presented. These characteristics are utilized in the development of the proposed control scheme and contribute to a noncomplex constant motor power factor control scheme without using feedback current measurements.

The drive voltage phasors $\vec{v}_1$ and $\vec{v}_2$ (see Fig. 1) represent the two components of the motor's per-phase fundamental voltage resulting from the main and floating bridge inverters, respectively. The fundamental phase difference between $\vec{v}_1$ and $\vec{v}_2$ is denoted by the angle α. In this work, α is kept constant at 90°, such that the main converter and floating converter supply real power and reactive power to the motor, respectively. $\vec{v}_m$ is the per-phase fundamental voltage supplied to the stator's windings and is the vector sum of $\vec{v}_1$ and $\vec{v}_2$

$$|\vec{v}_1| = \frac{m_1 V_{\rm dc}}{2\sqrt{2}} \tag{1}$$

$$|\vec{v}_2| = \frac{1.15\, V_{\rm cap}}{2\sqrt{2}} \tag{2}$$

$$\vec{v}_m = \vec{v}_1 + \vec{v}_2. \tag{3}$$

$V_{\rm dc}$ and $V_{\rm cap}$ are the supply dc voltage and the floating capacitor's dc voltage, respectively. The amplitude modulation index of the main bridge inverter, m_1, is controllable, while the floating bridge's amplitude modulation index, m_2, is kept at its maximum value in order to minimize its capacitor's voltage, thus decreasing switching losses and stresses in the floating converter. Under the proposed control, decreasing m_2 would increase the floating bridge's capacitor voltage, hence increasing losses and voltage stresses; thus

$$m_2 = 1.15. \tag{4}$$

The adopted controller allows the floating capacitor's voltage to fluctuate and reach a steady-state level, related to the motor's load conditions: in steady state operation, the system's current phasor $\vec{i}_s$ is orthogonal to $\vec{v}_2$. Note that the floating bridge capacitance can be made small enough as to meet the transient response requirements of the motor: in simple terms, the capacitor size, together with appropriate controller settings, can be chosen so that the system's transient response can be fast enough to cope with the motor's transients. Variations in the capacitor's voltage are dependent on the instantaneous real power absorbed by the floating bridge during speed and load transients

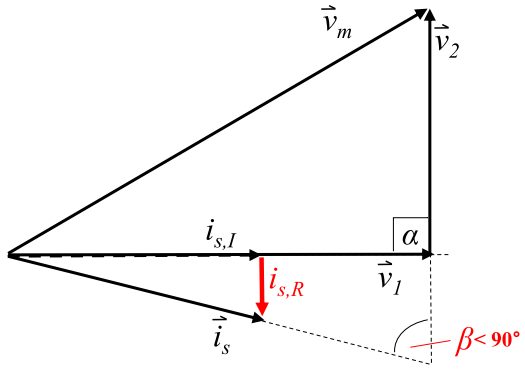

Fig. 2. Natural charging process of the floating capacitor.

$$P_2 = 3\,|\vec{v}_2|\left|\vec{i}_s\right|\cos\beta \tag{5}$$

where β is the angle formed between the vectors $\vec{i}_s$ and $\vec{v}_2$. $\vec{i}_s$ may be projected onto the axis of $\vec{v}_2$ resulting in real and imaginary components, $i_{s,R}$ and $i_{s,I}$. Assuming an ideal capacitor and power electronics, the real component of $\vec{i}_s$ will be zero when the system is at the steady state

$$i_{s,R}^{SS} = 0. \tag{6}$$

However, under practical conditions, the floating bridge will experience natural power losses such as the equivalent series resistance of the capacitor, as well as the switching and conduction losses in the power electronics. Under the steady state, these power losses result in the angle β, between $\vec{i}_s$ and $\vec{v}_2$, to be slightly less than 90°. For the remainder of the control scheme discussion, these power losses will be neglected and β will be assumed to be 90° under steady-state operation.

The floating capacitor transient charging process is depicted in Fig. 2. Since $\beta < 90°$, P_2 will be positive; thus, real power is absorbed by the floating bridge and the capacitor charges. Therefore, $|\vec{v}_2|$ will increase with the capacitor's voltage, moving $\vec{v}_m$ and $\vec{i}_s$ counterclockwise in the figure, until $i_{s,R}$ reaches zero. The complementary capacitor discharging process is demonstrated in Fig. 3. Both the power factor angle of the motor and the magnitude of $\vec{v}_1$ directly influence the angle β and thus, influence the steady-state voltage level of the floating capacitor. While the motor's power factor angle is highly dependent on the motor's loading conditions, it is also dependent on the motor's voltage. The magnitude of $\vec{v}_1$ is controlled by m_1, and the latter can be used as a control parameter to effectively regulate the floating bridge's capacitor voltage and, hence, the output voltage $|\vec{v}_2|$. For example, if the system is operating at steady

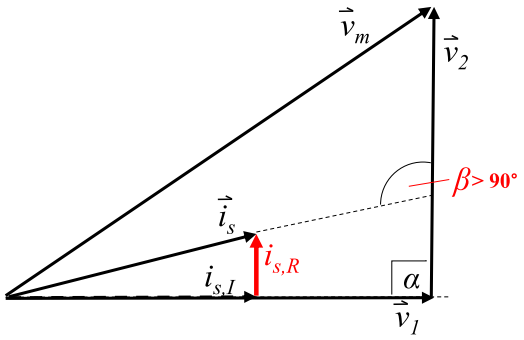

Fig. 3. Natural discharging process of the floating capacitor.

state and the capacitor voltage is to be increased, the controller increases m_1, hence $|\vec{v}_1|$ (see Fig. 2). This action causes the angle β to decrease slightly from 90°, as $\vec{i}_s$ lags behind $\vec{v}_1$. With β less than 90°, real power will flow into the floating bridge and charge the capacitor according to (5). Conversely, m_1, hence $|\vec{v}_1|$, is decreased to lower the floating capacitor's voltage (see Fig. 3).

III. High Motor Efficiency Using Power Factor Control

Justification for constant motor power factor control in a variable-frequency drive is presented. The proposed controller may be separated into two main components: power factor control and capacitor voltage control. A sensorless method for motor slip frequency compensation is also described.

Maximizing the power conversion efficiency of the induction motor has many benefits for improving the operational lifetime of the machine and lowering the power drawn from the dc supply [19], [30], [31]. Oversizing motors in industry is a common practice, which often leads to very low operating power factors and poor efficiencies [32]. In particular, an industry survey concluded that 29% of induction motors installed in 1992 were regularly operated at less than 50% load [33]. Therefore, a system that automatically operates the motor at its maximum efficiency point, regardless of load, could realize large energy savings and extend the lifetime of the machine. The maximum motor operating efficiency can be linked to many potential control parameters, but, for this work, it is linked to the machine operating with a constant power factor by controlling the motor's voltage [34], [35]. Improving a motor's power factor through voltage variation is a well-known technique used to maintain reasonable slip throughout operation [34]. Furthermore, it has been demonstrated that using a constant displacement power factor control scheme over an entire operating range is an effective efficiency optimization strategy in medium-sized industrial drives [35]. The optimal power factor for the IM will vary over the machine's speed and load range, and selecting the average power factor from the optimal range of values results in near minimized losses for all operating points [35]. In simplistic terms, the magnetizing inductance of the induction motor is considered to be in parallel to the rotor circuit, which is largely resistive. Balancing the motor's magnetizing current with the torque producing rotor current corresponds to a power factor

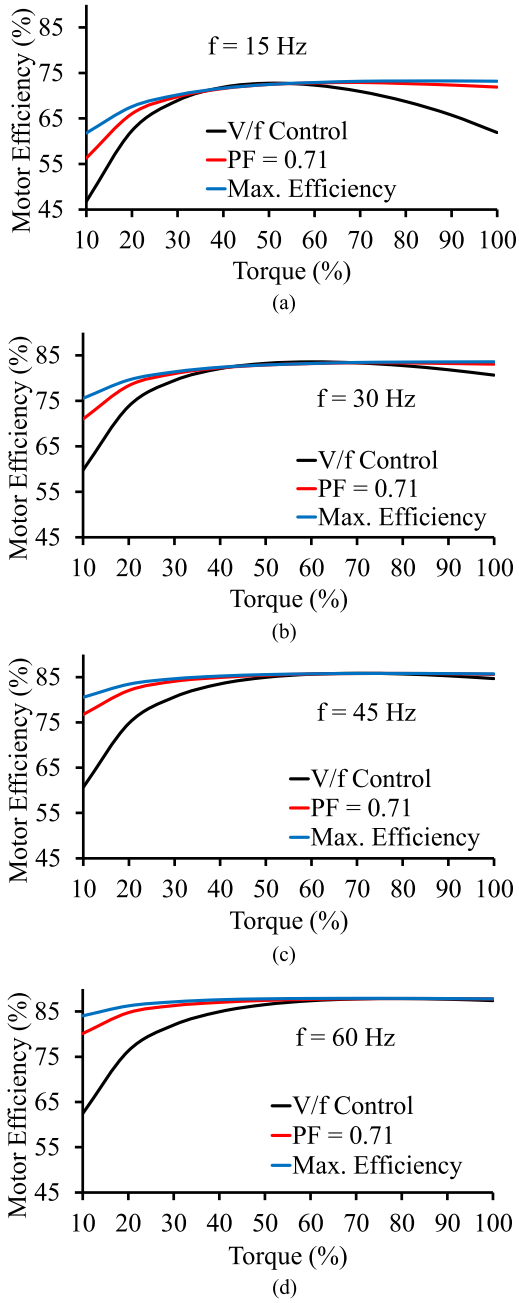

Fig. 4. Theoretical motor efficiencies at (a) 15 Hz, (b) 30 Hz, (c) 45 Hz, and (d) 60 Hz [100% torque = 20 N·m].

of approximately 0.71. Motor voltage control can improve the motor's power conversion efficiency by controlling its operating power factor: essentially controlling the balance between its iron and Cu losses. While a constant power factor setpoint of 0.71 was selected for the test motor used in this work, the optimal power factor for minimizing overall losses varies slightly between motors. High motor operating efficiencies can result throughout a wide range of drive operating frequencies and load conditions.

For a 5-hp experimental motor, Fig. 4 compares the theoretical efficiencies between using constant power factor control and the maximum possible motor operating efficiency. The

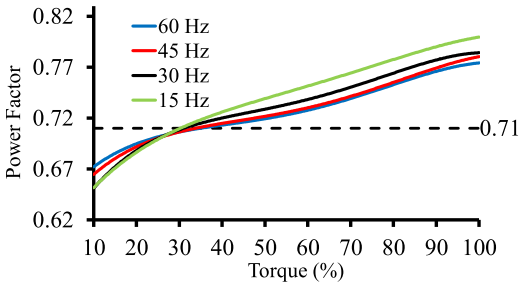

Fig. 5. Power factors for optimal efficiency operation for a 5-hp test motor.

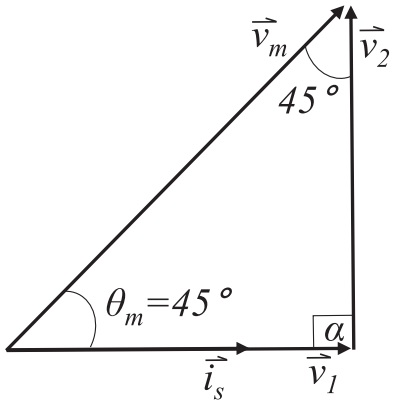

Fig. 6. Steady-state space-vector diagram.

theoretical efficiencies for various operating conditions and control methods were calculated using the equivalent circuit model for the IM and the parameters for the motor used in this work. For the motor used, 0.71 power factor control achieves motor efficiencies very close to the maximum possible, with a deviation under light loads. For completeness, the two operating conditions in Fig. 4 are also compared with *V/f* control. Fig. 5 displays the theoretical power factors that correspond to maximum efficiency operation at the specified speed setpoints. A power factor of 0.71 is within the range of optimal power factors. This value was selected, as opposed to the mean value in the optimal power factor range, as motor efficiency is more sensitive to power factor variation under light loads. These results justify the use of a relatively simplistic motor voltage control that keeps the motor operating at a constant power factor under variable-frequency and variable-load operation. The ideal constant power factor may vary slightly between motors, typically being nearer to the range of 0.70–0.75. This control approach is very well suited for the drive structure being used: the main bridge and floating bridge DID topology.

The proposed controller keeps the angle α at 90° for steady-state operation under all conditions (see Fig. 6). This results in the motor's current to be in phase with $\vec{v}_1$, resulting in unity power factor operation of the main bridge.

The controller incorporates two cascaded PI compensators (see Fig. 7). The PI block in the *"slower"* outer control loop works to control the ratio between $|\vec{v}_1|$ and $|\vec{v}_2|$ determined by measuring the dc voltages of both inverters and knowing their amplitude modulation indices m_1 and m_2. A fixed ratio between $|\vec{v}_1|$ and $|\vec{v}_2|$ is maintained by regulating the reference signal V^*_{cap} for the floating bridge's capacitor voltage, which is limited between 0 and V_{dc}. This fixed ratio is determined by the reference motor power factor, which may be updated in the control scheme based on the gain factor *K*:

$$K = 1/\tan\left[\cos^{-1}\left(\text{PF}^*\right)\right]. \tag{7}$$

For the motor utilized in this work, the desired motor power factor angle is $\theta_m = 45°$; thus, the value of the gain factor *K* equals 1 and the ratio of $|\vec{v}_1|$ to $|\vec{v}_2|$ is set to 1:1. However, this ratio could be altered in the control algorithm to obtain a wide range of desired motor power factors. V^*_{cap} provides the input signal to the *"faster"* inner control loop. The inner PI block minimizes the floating capacitor's voltage error by controlling m_1: limited between 0 and 1.15. The magnitude of $\vec{v}_1$ directly influences the charging and discharging of the floating capacitor. Equations in the Laplace domain for both PI compensators are as follows:

$$V^*_{\text{cap}} = \left(|\vec{v}_1| - K\,|\vec{v}_2|\right)\left(\frac{K_{p1}s + K_{i1}}{s}\right) \tag{8}$$

$$m_1 = \left(V^*_{\text{cap}} - V_{\text{cap}}\right)\left(\frac{K_{p2}s + K_{i2}}{s}\right). \tag{9}$$

K_{p1} and K_{p2} are the proportional gains and K_{i1} and K_{i2} are the integral gains for the primary and secondary PI compensators, respectively. Each compensator requires unique gains, as the bandwidth of the inner control loop must be large enough to track the output of the outer power factor control loop, while quickly rejecting disturbances in the capacitor's voltage. In other words, the inner loop gains are tuned according to the size of the floating capacitor and its corresponding *dv/dt* characteristics, whereas the outer loop gains are tuned according to the time constant of the motor and its dynamic response to load transients.

The motor's rpm reference is supplied to the control system and is boosted by a slip frequency compensation value before being converted into a reference supply frequency (see Fig. 7). Constant motor power factor control enables a simple method for slip compensation, in which a motor-specific rpm compensation value may remain constant for all operation. Thus, the DID topology is well suited for slip frequency compensation, providing a method for more accurate speed control without using speed feedback measurements. For example, the test motor utilized in this work has a slip of 23 r/min while operating at a power factor of 0.71. Thus, by forcing the input power factor and θ_m to be constant, the motor's slip frequency will also remain constant at all speed settings. Under experimental conditions, machine parameters will shift at varying temperatures caused by load fluctuations, thus creating small steady-state speed errors varying over the load range. Finally, an external triggered integrator is utilized to produce the reference phase angles for both bridges, which are sent to the corresponding space-vector PWM modulators.

Under this control, the DID can boost the motor voltage 41% higher than when using a single bridge, although the maximum practical motor voltage is limited by the internal flux saturation

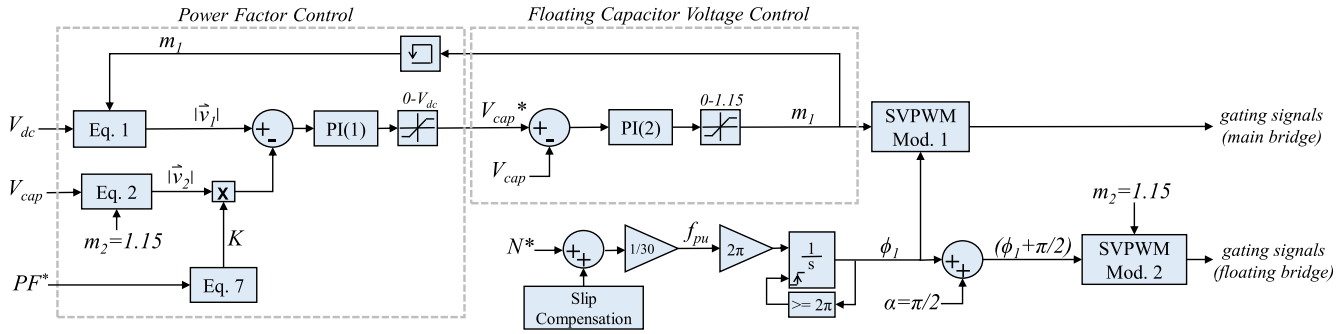

Fig. 7. Control block diagram.

TABLE I
INDUCTION MOTOR PARAMETERS

P_{rated}	=	3.73 kW	R_s	=	0.300	Ω
$I_{s,\text{rated}}$	=	13 A	R_R	=	0.244	Ω
$V_{s,\text{rated}}$	=	230 V	X_s	=	0.697	Ω
f_s	=	60 Hz	X_R	=	0.544	Ω
p	=	2	X_M	=	19.671	Ω

effects of the motor. The additional available voltage extends the base speed range of the drive and lessens the requirement for flux weakening, thus allowing for higher torque production at high speeds and better utilization of the motor's capabilities. In addition, the proposed regulation of V_{cap} significantly improves the floating capacitor's voltage stability during transient load and frequency changes. Under light loads and low drive frequencies, the terminal motor voltage for the chosen nominal power factor is greatly reduced. Thus, V^*_{cap} is reduced automatically, m_1 is reduced to track V^*_{cap}, and both $|\vec{v}_1|$ and $|\vec{v}_2|$ decrease in a proportional manner.

IV. Experimental Setup

Experimental testing conducted verifies the benefits of running the induction motor under constant power factor operation. A four-pole, 230-V, 5-hp, 20-N·m, 60-Hz, class H induction motor was tested at four drive frequencies: 15, 30, 45, and 60 Hz. In addition to the steady-state frequencies tested, the drive proved robust when subjected to a multitude of motor load and drive frequency transients. The rated nameplate parameters for the test motor are included in Table I.

Custom power electronics used Semikron (SKiM306GD12 E4) insulated-gate bipolar transistor (IGBT) modules with a 4-mF floating capacitor. A 300-V Xantrex dc supply (XPR 300-20) was utilized to supply the main bridge. A MAGTROL dynamometer was used to load the motor, and the test system was controlled using the dSPACE DS1104 controller board (see Fig. 8).

V. System Performance

In addition to experimental testing, the proposed controller for the DID was simulated in order to verify constant power factor operation and the regulation of the floating capacitor's voltage. Conducted simulations assumed an input dc supply voltage of 300 V, floating capacitors with capacitances of 12, 4, and 1 mF, and a switching frequency of 7.5 kHz. The drive control was proven to be effective by maintaining the nominal motor power factor of 0.71 for loads varying between zero and full load and over a supply frequency range of 10–75 Hz.

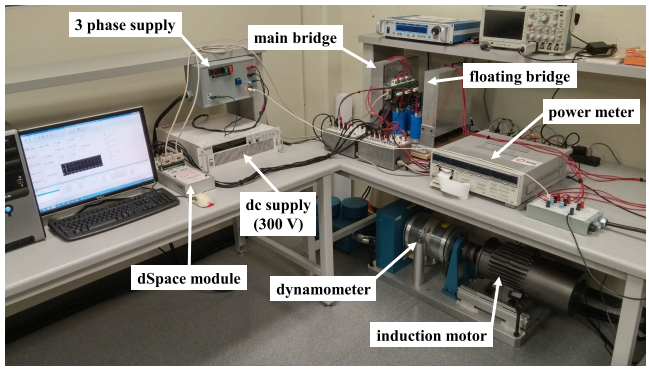

Fig. 8. Experimental setup.

A. Steady-State Performance

The motor's power conversion efficiency was obtained at the four drive frequencies tested, with the motor efficiency compared between the proposed controller, maximum theoretical efficiency operation, and constant *V/f* control (see Fig. 9). For the purpose of this paper, conventional *V/f* control is utilized as a low benchmark standard, while the goal of the system is to achieve motor efficiencies close to the theoretical maximum values at various steady-state operating points. The theoretical maximum efficiencies were calculated using the equivalent circuit model for the induction motor, while accounting for thermal variations in the motor's parameters across varying loads. The 300-V dc source utilized in the experimental setup was not sufficient to supply the motor its rated voltage under 60-Hz operation from a single-inverter drive for *V/f* control; thus, the motor was supplied directly at its rated voltage from a 60-Hz source with no power electronics in this scenario. However, the inherent voltage-boosting capability of the DID enabled the use of the 300-V dc supply under constant power factor 60-Hz operation at all motor loads. This example further illustrates the usefulness of the DID's voltage-boosting capability while operating from a limited dc supply voltage.

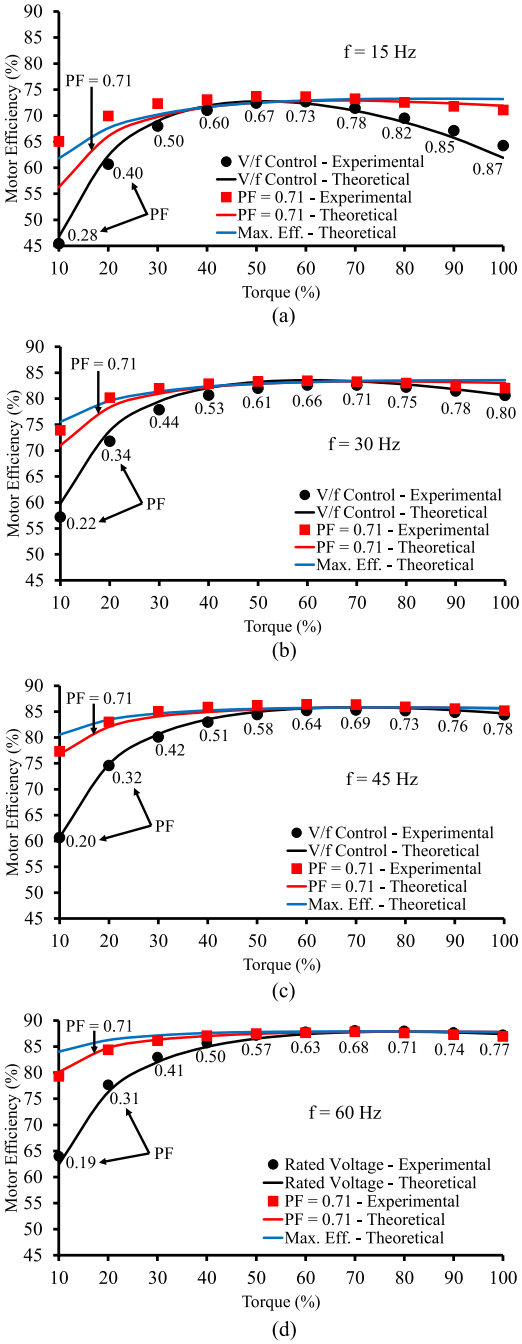

Fig. 9. Experimental results: motor efficiencies under *V/f* control and constant power factor control compared with the theoretical maximum motor efficiencies at (a) 15 Hz, (b) 30 Hz, (c) 45 Hz, and (d) 60 Hz.

First, the data show good agreement between the theoretical and experimental results. Rated voltage *V/f* control results in large motor efficiency variations with load drooping slightly at high loads and with a significant decrease under light-load conditions. The power conversion efficiencies are highest under 60-Hz operation and decrease with each drive frequency setting. The *V/f* efficiencies peak in the mid-torque regions, which coincide with the constant power factor operation curves. The constant power factor controller results in elevated motor efficiencies compared to *V/f* control, remaining fairly constant with

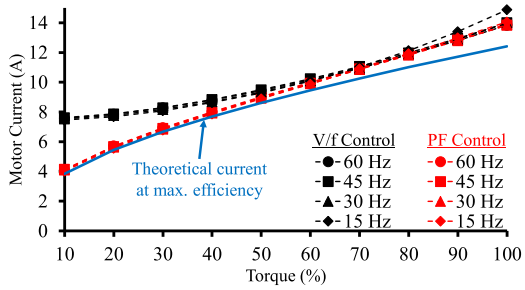

Fig. 10. Experimental results: motor current comparison between constant power factor control, *V/f* control, and theoretical maximum efficiency operation.

load settings, before beginning to droop at approximately 30% load. The largest efficiency gains are observed under 15-Hz operation, in which constant power factor control shows increases over *V/f* control of approximately 18% and 7% at 10% and 100% loads, respectively. Most importantly, as predicted under constant power factor control, the motor efficiency remains very close to the theoretical maximum power conversion efficiencies. The largest negative discrepancies between the measured experimental efficiency and the theoretical maximum efficiency occurred at 10% load during 45- and 60-Hz operation, at roughly 4% decrease. At the supply frequencies of 15 and 30 Hz, there is an approximate 1.5% decrease in efficiency from the theoretical maximum at full load. These discrepancies are expected based upon the theoretical predictions, as the motor's optimal power factor is shown to vary over its operating range (see Fig. 5).

The current drawn by the motor also demonstrates the benefits of the proposed drive controller. At the drive frequencies tested, the constant power factor control strategy results in a lower motor current than conventional *V/f* control at motor loads less than 60% (see Fig. 10). The greatest decrease in current is observed at 10% load, at which the motor current is reduced by nearly 4 A, resulting from very poor power factors at low loads produced by *V/f* control. Furthermore, the constant power factor controller results in motor currents very close to the theoretical minimum values at below 60% load. At above 60% load, the equivalent circuit model utilized predicts motor currents slightly below the measured values, with a difference of 1.6 A at full load. Minimizing the motor current both decreases the conduction losses in the system and lowers the temperature of the motor.

Steady-state voltage measurements of the motor phase voltage and floating capacitor voltage demonstrate the action of the proposed control (see Fig. 11). Under 60-Hz operation and at rated load, the controller supplied a voltage boost of 8% beyond the motor's rated voltage in order to maintain the desired power factor (20% beyond the voltage capability of the single inverter drive). Thus, this topology can extend the base speed range of the drive and improve motor performance at high speeds compared to a single-inverter drive. At reduced motor loads and drive operating frequencies, $|\vec{v}_1|$ and $|\vec{v}_2|$ are reduced in a proportional manner through the reduction of m_1 and V_{cap}. The proposed controller automatically reduces the motor supply voltage to maintain the desired operating power factor under light loads. Theoretical expected values for the motor phase voltage and floating capacitor voltage were calculated using the motor's

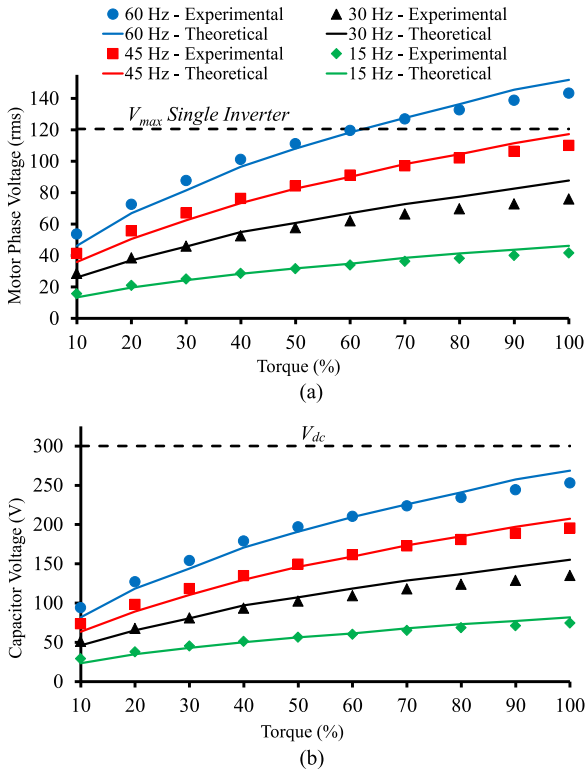

Fig. 11. Experimental results. (a) Motor phase rms voltage and (b) floating capacitor voltage of the DID under constant power factor control.

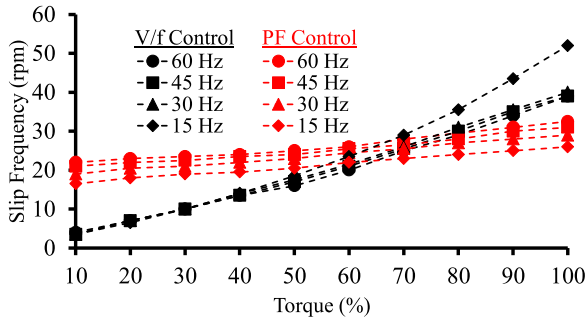

Fig. 12. Experimental results: motor rpm slip comparison between constant power factor and *V/f* control methods.

equivalent circuit model and the drive's topology, resulting in similar trends to the measured values.

The slip variation over the entire load range is greatly reduced under the proposed controller compared to the conventional *V/f* control scheme (see Fig. 12). Constant power factor operation results in a slip variation of approximately 10 r/min between 10% and full load at each frequency setting. Theoretically, the motor slip remains constant across all motor loads; however, motor temperature fluctuations and varying switching losses in the power electronics result in small errors in the aforementioned steady-state assumptions. Essentially, the switching, conduction and capacitor losses of the floating bridge cause the angle β between vectors $\vec{i}_s$ and $\vec{v}_2$ to be slightly less than 90°, thus producing a nonzero $i_{s,R}$ value at the steady state and violating the assumption of (6). For the test motor utilized, a slip compensation value of 23 r/min (1.28% at rated speed) results

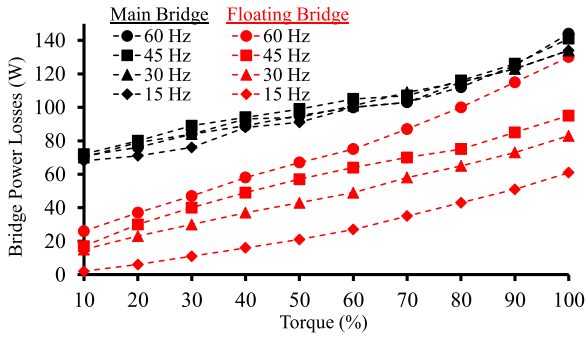

Fig. 13. Experimental results: power losses in the main and floating bridges.

in a maximum steady-state speed error of 7 r/min over all drive operating points tested, representing an error of 0.39% of the rated motor speed.

An additional benefit of lowering V_{cap} under light loads and low speeds is a reduction in the switching losses in the floating bridge. Device switching losses are proportional to both the device current and the dc-link voltage. This reduction of V_{cap} lowers the switching losses in the electronics of the floating converter (see Fig. 13). Mainly due to conduction losses, the power losses in the main bridge decrease with current almost linearly from full load to zero load for the four drive frequencies tested. However, in addition to varying with the load current, the losses in the floating bridge decrease significantly at each frequency, primarily due to reduced switching losses from a reduced dc capacitor voltage. The difference between the main and floating bridges represents a power saving due to the fluctuation of the floating capacitor's voltage, resulting in a more efficient system than if the floating capacitor remained equal to the input dc-link voltage throughout all operation. This justifies maintaining the modulation index of the floating bridge at its maximum value as stated by (4).

B. System Start-Up Procedure

The system start-up procedure is comprised of three stages. First, the motor is started using a conventional soft-start current-limiting method from solely the main converter [36]. The three upper IGBT switches of the floating converter remain closed during this process in order to emulate a *Y*-connection at the motor's secondary terminals. Second, switching in the floating converter is enabled, and the capacitor is precharged to a predetermined value using the second PI compensator of the control algorithm. Under 60-Hz operation, the magnitude of V^*_{cap} upon precharging was set to 100 V (see Fig. 14). Finally, the power factor control portion of the control scheme is enabled, thus allowing the first PI compensator to update V^*_{cap} appropriately corresponding to the drive's current frequency and load conditions.

C. Load Transient Stability

To demonstrate the controller's response to transient load changes, both simulation and experimental results are included for positive and negative step changes in the motor's load.

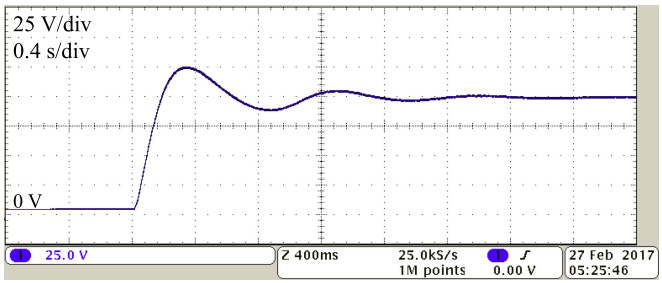

Fig. 14. Experimental results: capacitor precharging (4-mF floating capacitor).

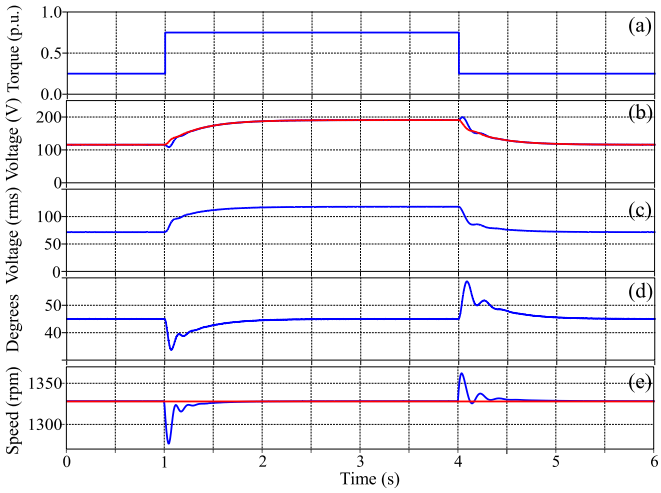

Fig. 15. Simulation results. (a) Load torque. (b) Capacitor voltage (blue) and reference (red). (c) Motor phase voltage. (d) Motor power factor angle. (e) Motor speed (blue) and reference (red) (45 Hz; 1 mF floating capacitor).

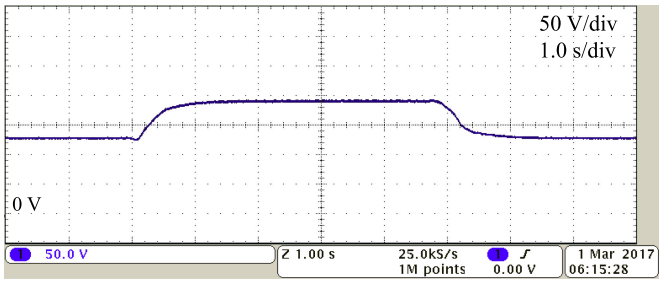

Fig. 16. Experimental results: floating capacitor voltage during load transients (45 Hz; 4-mF floating capacitor).

Simulation results show the system's capacitor voltage, motor voltage, motor's power factor angle, and speed (see Fig. 15). Identical load step changes were supplied to the experimental setup, demonstrating a stable floating capacitor voltage throughout the transient conditions (see Fig. 16). Further selected experimental results include m_1, $|\vec{v}_1|$ and $|\vec{v}_2|$, and the rms motor current $|\vec{i}_s|$ (see Fig. 17). At the positive load step change, $|\vec{v}_m|$ automatically increases to maintain the motor's nominal power factor. The first PI block increases V^*_{cap} to maintain the 1:1 ratio between $|\vec{v}_1|$ and $|\vec{v}_2|$. The second PI block increases m_1 to track V^*_{cap}, causing both $|\vec{v}_1|$ and $|\vec{v}_2|$ to increase. The motor's power factor angle and speed initially decrease after the load increase, before returning to nominal values. Once the transient event has

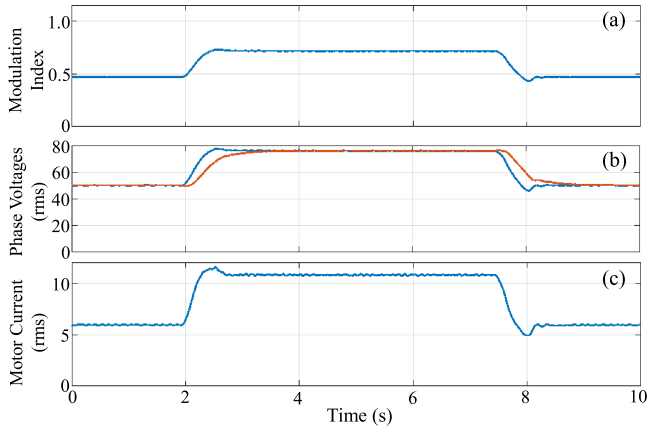

Fig. 17. Experimental results. (a) Modulation index, m_1. (b) Phase voltages $|\vec{v}_1|$ (blue) and $|\vec{v}_2|$ (red). (c) RMS motor current, $|\vec{i}_s|$ (45 Hz; 4-mF floating capacitor).

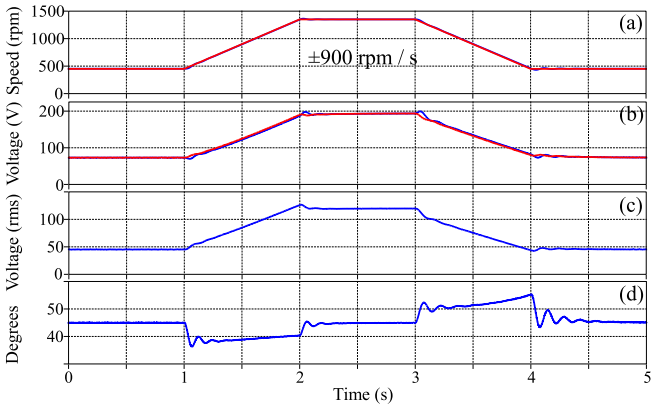

Fig. 18. Simulation results. (a) Motor speed (blue) and reference (red). (b) Capacitor voltage (blue) and reference (red). (c) Motor phase voltage. (d) Motor power factor angle (0.75-p.u. load; 1-mF floating capacitor).

finished, the system will reach a new steady-state operating point with a higher dc-link voltage at the floating bridge. The behavior of the floating capacitor's voltage throughout the transient events demonstrates stable dynamic system performance.

D. *Speed Transient Stability*

Similarly, the system's response to speed transients is demonstrated through both simulation and experimental results. Fig. 18 shows simulation results for the motor's input reference speed, capacitor voltage, motor voltage, and power factor angle. Identical speed transients were applied to the experimental system, demonstrating a stable capacitor voltage throughout the transients (see Fig. 19). Further selected experimental results include m_1, $|\vec{v}_1|$ and $|\vec{v}_2|$, and $|\vec{i}_s|$ (see Fig. 20). As the reference speed increases, the first PI block increases V^*_{cap} linearly to maintain the desired power factor of the motor. The second PI block tracks V^*_{cap} by varying m_1. The motor's power factor angle is not maintained at the desired 45° during the speed transient due to the inherent transient response of the motor and the limitations of the PI compensators. Once the speed transient is complete, the floating capacitor settles at a new steady-state

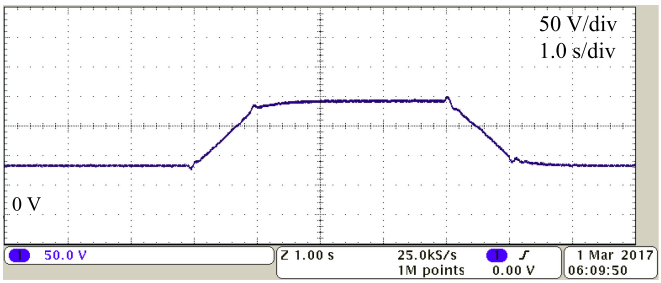

Fig. 19. Experimental results: floating capacitor voltage during speed transients (0.75-p.u. load; 4-mF floating capacitor).

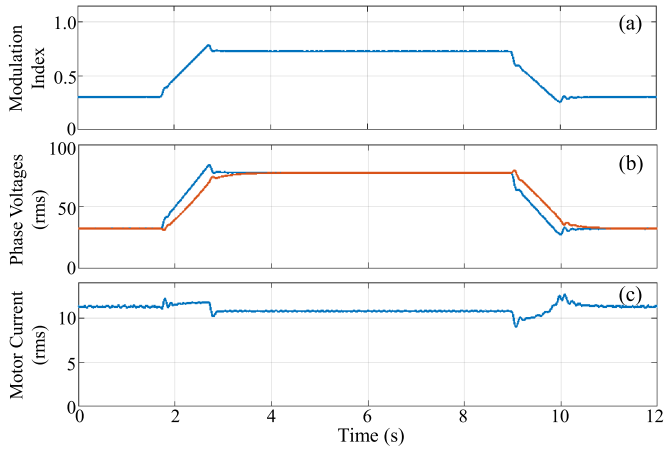

Fig. 20. Experimental results. (a) Modulation index, m_1. (b) Phase voltages $|\vec{v}_1|$ (blue) and $|\vec{v}_2|$ (red). (c) RMS motor current, $|\vec{i}_s|$ (0.75-p.u. load; 4-mF floating capacitor).

voltage, and the motor's nominal power factor angle is once again achieved.

VI. Conclusion

The proposed drive control is successfully demonstrated for an open-ended winding induction motor drive system using a DID with a floating capacitor bridge. The controller maintains the motor's nominal power factor over a wide range of loading conditions and drive frequencies, while also regulating the floating capacitor's voltage at a stable value. Experimental testing of the controller verified near-optimal motor efficiencies over a wide load range and showed large efficiency gains when compared to a constant *V/f* control scheme. Furthermore, the proposed control was shown to be robust and stable through both motor load and speed transients in terms of motor operation and capacitor voltage stability, demonstrating good suitability for dynamic drives. To achieve higher performance dynamic characteristics, a more complex field-oriented current control approach is recommended due to the limitations of scalar control. Varying the voltage reference of the floating capacitor reduced the switching losses of the floating bridge at low speeds and light loads, thus further improving the system's overall power conversion efficiency. The DID topology was shown to be well suited for slip frequency compensation, providing a method for more accurate speed control without using speed feedback measurements. The constant slip frequency compensation method, incorporating a motor-specific rpm value, allowed for sensorless speed regulation of the open-ended winding induction motor within 0.39% of the rated motor speed for all drive operating points tested. The proposed control algorithm is well suited to be extended to a more complex rotor field-oriented control scheme, in which the motor's displacement power factor is controlled directly by the injected stator current, as opposed to being controlled indirectly by the ratio of the fundamental bridge voltages. Under this scenario, the floating capacitor voltage may fluctuate naturally depending on the motor's operating conditions or be regulated using the secondary bridge. Thus, the knowledge of rotor position could potentially facilitate the further enhancement of the drive's dynamic characteristics.

References

[1] A. Edpuganti and A. Rathore, "New optimal pulsewidth modulation for single dc-link dual-inverter fed open-end stator winding induction motor drive," *IEEE Trans. Power Electron.*, vol. 30, no. 8, pp. 4386–4393, Aug. 2015.

[2] J. Ewanchuk, J. Salmon, and C. Chapelsky, "A method for supply voltage boosting in an open-ended induction machine using a dual inverter system with a floating capacitor bridge," *IEEE Trans. Power Electron.*, vol. 28, no. 3, pp. 1348–1357, Mar. 2013.

[3] J. Ewanchuk and J. Salmon, "A square-wave controller for high speed induction motor drive using a three phase floating bridge inverter," in *Proc. IEEE Energy Convers. Congr. Expo.*, 2010, pp. 2584–2591.

[4] R. Haque, A. Kowal, J. Ewanchuk, A. Knight, and J. Salmon, "PWM control of a dual inverter drive using an open-ended winding induction motor," in *Proc. IEEE Appl. Power Electron. Conf. Expo.*, 2013, pp. 150–156.

[5] S. Chowdhury, P. Wheeler, C. Patel, and C. Gerada, "A multilevel converter with a floating bridge for open-ended winding motor drive applications," *IEEE Trans. Ind. Electron.*, vol. 63, no. 9, pp. 5366–5375, May 2016.

[6] S. Chowdhury, P. Wheeler, C. Gerada, and C. Patel, "Model predictive control for a dual-active bridge inverter with a floating bridge," *IEEE Trans. Ind. Electron.*, vol. 63, no. 9, pp. 5558–5568, May 2016.

[7] S. Chowdhury, P. Wheeler, C. Gerada, and S. Arevalo, "A dual inverter for an open end winding induction motor drive without an isolation transformer," in *Proc. IEEE Appl. Power Electron. Conf. Expo.*, 2015, pp. 283–289.

[8] S. Chowdhury, P. Wheeler, C. Gerada, and C. Patel, "A dual two-level inverter with a single source for open end winding induction motor drive application," in *Proc. 17th Eur. Conf. Power Electron. Appl.*, 2015, pp. 1–9.

[9] H. Kubo, Y. Yamamoto, T. Kondo, K. Rajashekara, and B. Zhu, "Zero-sequence current suppression for open-end winding induction motor drive with resonant controller," in *Proc. IEEE Appl. Power Electron. Conf. Expo.*, 2016, pp. 2788–2793.

[10] V. Oleschuk, V. Ermuratski, F. Profumo, A. Tenconi, R. Bojoi, and A. M. Stankovic, "Novel schemes of synchronous PWM for dual inverter-fed drives with cancellation of the zero sequence currents," in *Proc. IEEE Int. Symp. Power Electon., Elect. Drives Autom. Motion*, 2006, pp. 451–456.

[11] K. Ramachandrasekhar, S. Mohan, and S. Srinivas, "An improved PWM for a dual two-level inverter fed open-end winding induction motor drive," in *Proc. Int. Conf. Elect. Mach.*, 2010, pp. 1–6.

[12] V. T. Somasekhar, S. Srinivas, B. P. Reddy, C. N. Reddy, and K. Sivakumar, "Pulse width-modulated switching strategy for the dynamic balancing of zero-sequence current for a dual-inverter fed open-end winding induction motor drive," *IET Electr. Power Appl.*, vol. 1, no. 4, pp. 591–600, Jul. 2007.

[13] Y. Zhao and T. Lipo, "Space vector PWM control of dual three-phase induction machine using vector space decomposition," *IEEE Trans. Ind. Appl.*, vol. 31, no. 5, pp. 1100–1109, Sep. 1995.

[14] D. Casadei, G. Grandi, A. Lega, C. Rossi, and L. Zarri, "Switching technique for dual-two level inverter supplied by two separate sources," in *Proc. IEEE Appl. Power Electron. Conf. Expo.*, 2007, pp. 1522–1528.

[15] G. Grandi and D. Ostojic, "Dual inverter space vector modulation with power balancing capability," in *Proc. IEEE EUROCON*, 2009, pp. 721–728.
[16] D. Casadei, G. Grandi, A. Lega, and C. Rossi, "Multilevel operating and input power balancing for a dual two-level inverter with insulated DC sources," *IEEE Trans. Ind. Appl.*, vol. 44, no. 6, pp. 1815–1824, Nov. 2008.
[17] E. G. Shivakumar, K. Gopakumar, S. K. Sinha, A. Pittet, and V. T. Ranganathan, "Space vector PWM control of dual inverter fed open-end winding induction motor drive," in *Proc. IEEE Appl. Power Electron. Conf. Expo.*, 2001, pp. 399–405.
[18] J. Kalaiselvi, K. R. Sekhar, and S. Srinivas, "Common mode voltage elimination PWMs for a dual two-level VSI with single inverter switching," in *Proc. IEEE Int. Symp. Ind. Electron.*, 2012, pp. 234–239.
[19] J. Kim, J. Jung, and K. Nam, "Dual-inverter control strategy for high-speed operation of EV induction motors," *IEEE Trans. Ind. Electron.*, vol. 51, no. 2, pp. 312–320, Apr. 2004.
[20] J. S. Park and K. Nam, "Dual inverter strategy for high speed operation of HEV permanent magnet synchronous motor," in *Proc. IEEE Ind. Appl. Conf.*, 2006, pp. 488–494.
[21] M. Mengoni, A. Tani, L. Zarri, G. Rizzoli, G. Serra, and D. Casadei, "Control of an open-ended induction machine using a dual inverter system with a floating capacitor bridge," in *Proc. IEEE Energy Convers. Congr. Expo.*, 2015, pp. 4872–4879.
[22] M. Mengoni, A. Amerise, L. Zarri, A. Tani, G. Serra, and D. Casadei, "Robust control of an open-ended induction motor drive with a floating capacitor bridge over a wide speed range," in *Proc. IEEE Energy Convers. Congr. Expo.*, 2016, pp. 1–7.
[23] B. A. Welchko, T. A. Lipo, T. M. Jahns, and S. E. Schulz, "Fault tolerant three-phase AC motor drive topologies: A comparison of features, cost, and limitations," *IEEE Trans. Power Electron.*, vol. 19, no. 4, pp. 1108–1116, Jul. 2004.
[24] E. Levi, "Multiphase electric machines for variable-speed applications," *IEEE Trans. Ind. Electron.*, vol. 55, no. 5, pp. 1893–1909, Apr. 2008.
[25] S. Kouro, J. Rodriguez, W. Bin, S. Bernet, and M. Perez, "Powering the future of industry: High-power adjustable speed drive topologies," *IEEE Ind. Appl. Mag.*, vol. 18, no. 4, pp. 26–39, May 2012.
[26] E. Levi, M. Jones, and W. Satiawan, "A multiphase dual-inverter supplied drive structure for electric and hybrid electric vehicles," in *Proc. IEEE Veh. Power Propulsion Conf.*, 2010, pp. 1–7.
[27] N. Bodo, M. Jones, and E. Levi, "PWM techniques for an open-end winding fivephase drive with a single DC source supply," in *Proc. IEEE Conf. Ind. Electron. Soc.*, 2012, pp. 3641–3646.
[28] M. R. Baiju, K. K. Mohapatra, R. S. Kanchan, and K. Gopakumar, "A dual two-level inverter scheme with common mode voltage elimination for an induction motor drive," *IEEE Trans. Power Electron.*, vol. 19, no. 3, pp. 794–805, May 2004.
[29] I. Smith, R. U. Haque, A. Tavakoli, and J. Salmon, "Power factor control for high efficiency operation of an open-ended winding motor using a dual inverter drive with a floating bridge," in *Proc. IEEE Appl. Power Electron. Conf. Expo.*, 2017, pp. 1935–1941.
[30] I. Tamrakar and O. P. Malik, "Power factor correction of induction motors using PWM inverter fed auxiliary stator winding," *IEEE Trans. Energy Convers.*, vol. 14, no. 3, pp. 426–432, Sep. 1999.
[31] Y. Yao, A. Cosic, and C. Sadarangani, "Power factor improvement and dynamic performance of an induction machine with a novel concept of a converter-fed rotor," *IEEE Trans. Energy Convers.*, vol. 31, no. 2, pp. 769–775, Jun. 2016.
[32] P. Pillay, "Applying energy-efficient motors in the petrochemical industry," *IEEE Ind. Appl. Mag.*, vol. 3, no. 1, pp. 32–40, Jan. 1997.
[33] E. B. Agamloh, "The partial-load efficiency of induction motors," *IEEE Trans. Ind. Appl.*, vol. 45, no. 1, pp. 332–340, Jan. 2009.
[34] R. Spee and A. K. Wallace, "Comparative evaluation of power factor improvement techniques for squirrel cage induction motors," *IEEE Trans. Ind. Appl.*, vol. 28, no. 2, pp. 381–386, Mar. 1992.
[35] F. Abrahamsen, F. Blaabjerg, J. K. Pedersen, and P. B. Thoegersen, "Efficiency-optimized control of medium-size induction motor drives," *IEEE Trans. Ind. Appl.*, vol. 37, no. 6, pp. 1761–1767, Nov. 2001.
[36] F. Blaabjerg, J. K. Pedersen, S. Rise, H. H. Hansen, and A. M. Trzynadlowski, "Can soft-starters help save energy?" *IEEE Ind. Appl. Mag.*, vol. 3, no. 5, pp. 56–66, Sep. 1997.

Ian J. Smith received the B.Eng. degree in sustainable and renewable energy engineering from Carleton University, Ottawa, ON, Canada, in 2015. He is currently working toward the M.Sc. degree in electrical engineering with the University of Alberta, Edmonton, AB, Canada, under the supervision of Dr. J. Salmon.

His research interests include induction and permanent magnet motor drives, multilevel converter topologies, and power electronics in renewable energy and grid-scale battery systems.

Mr. Smith was a recipient of Carleton University's Senate Medal for academic achievement and service to the engineering community. He is also a recipient of the National Science and Engineering Research Council's Undergraduate Student Research Award and the Canada Graduate Scholarship, as well as the Alberta Innovates Graduate Students Scholarship.

John Salmon (M'86) received the B.Sc. Eng. degree from Imperial College London, London, U.K., in 1982, the M.Eng. degree from McGill University, Montreal, QC, Canada, in 1984, and the Ph.D. degree from Imperial College London, London, U.K., in 1987, all in electrical engineering.

In 1987, he became an Assistant Professor with the Department of Electrical Engineering, University of Alberta, Edmonton, AB, Canada, where he has been a Full Professor since 1996. His current research interests include power converters for electric vehicles (machine-drive systems, grid interface, charging, and voltage balancing of batteries), high-speed generators, utility interface of wind generators, electrical energy storage including high-speed flywheels and batteries, coupled inductors for utility rectifiers and machine drive systems, and pulse-width-modulated techniques.

Dr. Salmon is a recipient of three Prize Paper Awards from the IEEE Industry Applications Society: the Industrial Drives Committee Award in 2008 and the Industrial Power Converter Committee Award in 2010 and 1994.